

Three mechanical models for blebbing and multi-blebbing

THOMAS E. WOOLLEY*, EAMONN A. GAFFNEY, SARAH L. WATERS, JAMES M. OLIVER, RUTH E. BAKER
AND ALAIN GORIELY

Mathematical Institute, University of Oxford, 24-29 St Giles, Oxford OX1 3LB, UK

*Corresponding author: woolley@maths.ox.ac.uk gaffney@maths.ox.ac.uk
waters@maths.ox.ac.uk oliver@maths.ox.ac.uk baker@maths.ox.ac.uk goriely@maths.ox.ac.uk

[Received on 19 July 2013; revised on 16 May 2014; accepted on 18 May 2014]

Membrane protrusions known as blebs play important roles in many cellular phenomena. Here we present three mathematical models of the bleb formation, which use biological insights to produce phenotypically accurate pressure-driven expansions. First, we introduce a recently suggested solid mechanics framework that is able to create blebs through stretching the membrane. This framework is then extended to include reference state reconfigurations, which models membrane growth. Finally, the stretching and reconfiguring mechanical models are compared with a much simpler geometrically constrained solution. This allows us to demonstrate that simpler systems are able to capture much of the biological complexity despite more restrictive assumptions. Moreover, the simplicity of the spherical model allows us to consider multiple blebs in a tractable framework.

Keywords: bleb; solid mechanics; cellular motion; semi-inverse problem.

1. Introduction

Cellular blebs are pressure-driven protrusions that occur when a cell's lipid bilayer membrane delaminates from its actin cortex (Charras, 2008) (see Fig. 1). Although for a long time, it was assumed that blebs were a sign of apoptosis (Russell *et al.*, 1972) it has been recently observed that blebs also play an important role in a number of other cellular phenomena, from mitosis (Prothero & Spencer, 1968) to locomotion in tumour, embryonic and stem cells (Keller & Bebie, 1996; Keller & Egli, 1998; Sahai & Marshall, 2003; Blaser *et al.*, 2006; Fackler & Grosse, 2008; Otto *et al.*, 2011). Because of its relevance to cellular mechanics, we will use mathematical models to provide quantitative insights into the mechanisms underlying bleb formation. In particular, we use non-linear elasticity to model the membrane's ability to undergo large deformations through growth and remodelling (Maugis *et al.*, 2010; Collins-Hooper *et al.*, 2012).

1.1 Biological background

Before a bleb forms (quiescent stage of Fig. 2) a cell's bilipid membrane is adhered to a porous mesh known as the cortex, which is made from polymerized actin chains (Charras, 2008). This membrane surrounds intracellular fluid known as cytosol, which is able to flow through the porous cortex. Myosin motors pull on the cortex–membrane adhesions causing the cytosol to be pressurized. If the cortex and/or the adhesions are disrupted, the pressurized cytosol will flow into the weakened section producing a protrusion, which is typically small and spherical (expansion stage of Fig. 2) (Cunningham, 1995).

Biologically, it is currently not known what triggers or controls the spatiotemporal appearances of blebs, although they can be initialized by external means (Tinevez *et al.*, 2009). The expansion phase

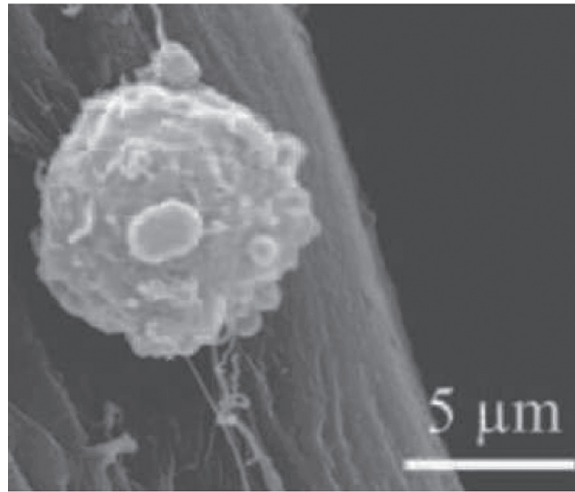


FIG. 1. Scanning electron microscope image of a blebbing cell (Collins-Hooper *et al.*, 2012).

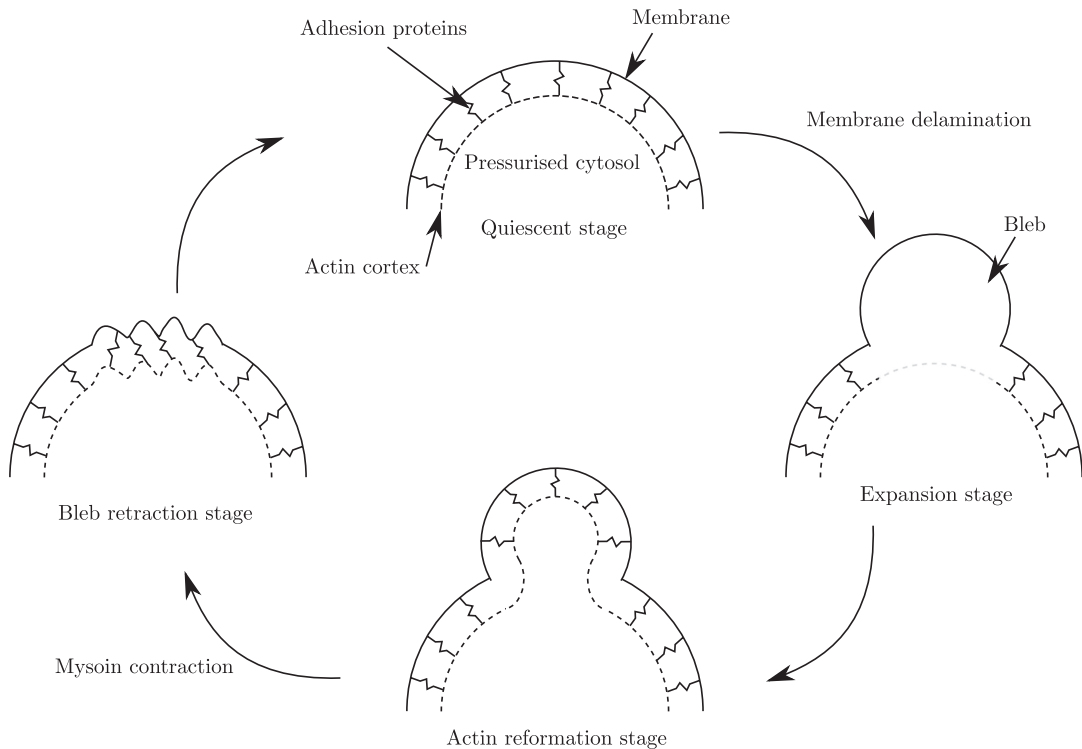


FIG. 2. Cyclical dynamics of a blebbing cell. Starting from a state in which the membrane and cortex adhere the membrane is able to break away from the cortex, allowing a bleb to form. The bleb expansion stops abruptly and the actin cortex reforms beneath the membrane. Slowly, the cortex buckles and deforms in such a way as to retract the protrusion. Note that the images are not to scale, as the adhesion protein spatial scale, $\sim 10^{-2} \mu\text{m}$, is much smaller than the cellular scale, $\sim 1 \mu\text{m}$.

can last anywhere from 5 to 30 s, with the final bleb size having a radius on the order of 1–4 μm (Charras *et al.*, 2008). In particular, we are interested in the blebs produced by muscle satellite stem cells (Otto *et al.*, 2011; Collins-Hooper *et al.*, 2012). These cells use blebs to migrate along muscle fibres, discover muscle damage and effect wound healing. In our previous theoretical study, we have shown that if cells create protrusions by only stretching their membrane, then the membrane must stretch by more than 100% in order to accommodate such bleb sizes (Woolley *et al.*, 2014). This is unrealistic as it is known that cellular membrane will tear after only a 4% increase in area (Hallett & Dewitt, 2007). Thus, local membrane growth must either occur through unravelling of invaginations or through exocytosis, whereby extra membrane is produced by polymerizing reactants in the cytosol. It has been estimated that there is at least 20–40% extra membrane available through each of these mechanisms and that the membrane can be produced in a matter of second (Charras *et al.*, 2008; Hallett *et al.*, 2008).

As quickly as blebbing begins, growth is halted and the membrane appears to enter a rest phase for 10–30 s (actin reformation stage of Fig. 2). While the biological basis for growth arrest is not known, it has been experimentally observed and theoretically argued that although the formation of blebs leads to a reduction in a cell's internal pressure, the pressure is still large enough to allow further blebs to form (Dai & Sheetz, 1999; Woolley *et al.*, 2014). Thus, pressure is not a limiting factor. Further, treatments with cytochalasin D have shown that abnormally large blebs can be induced quickly; thus, it does not appear that membrane growth is a limiting factor either (Cunningham, 1995). The current hypothesis is that the growth period is determined by the speed of actin cortex reformation and subsequent reattachment to the membrane. Over a much longer timescale of 1–2 min, the cortex contracts and deforms causing the bleb to be retracted and, thus, the cycle can begin again (bleb retraction phase of Fig. 2).

1.2 Previous mathematical approaches

Because blebbing occurs on such small spatial and temporal scales, it is particularly difficult to generate experimental insights into the mechanical processes. Thus, mathematical modelling can offer a framework within which hypotheses can be tested leading to focused experimental design. A number of mathematical frameworks have been proposed to model blebbing and we summarize these briefly below. It should be noted that due to the application of mathematics to blebbing being relatively new, no model completely reproduces a biologically accurate cycle of dynamics shown in Fig. 2. Instead, mathematical approaches have been varied as different groups have focused their attentions on characterizing specific aspects of the blebbing cycle. The first four models we introduce focus mainly on the expansion phase and production of the blebbed profile.

A very simple geometric description of blebbing is considered by Hu (2009). The model consists of two spherical caps continuously connected through their neck regions. The two spherical caps form the cell and bleb bodies, respectively. Although the total volume of the system is conserved the volume of the bleb spherical cap could be prescribed. Critically, by comparing the surface area of the blebbed form against the initial form, the authors noted that their model violates the 4% membrane area increase, after which they focused on protrusions within this limit.

An axisymmetric, solid mechanic model with linear stress–strain constitutive relations that did not consider bending stresses or the membrane's ability to grow was developed by Tinevez *et al.* (2009). By comparing their theoretical and experimental results, they were able to explain observed correlations between bleb size and membrane tension data. This enabled a prediction for a threshold value of surface tension, below which no blebs could nucleate.

Strychalski & Guy (2012) produced a 2D dynamic computational model of the cell that includes interactions between 1D curves, modelling the membrane and cortex, surrounding an intracellular fluid domain. The model was used to explore computationally the relationships between bleb formation time and cytoplasmic viscosity, reproducing quantitatively accurate results.

Spangler *et al.* (2011) considered a 3D model of the actin cortex using a triangulated mesh of particles coupled by springs. Further springs were added to create adhesion bonds between the cortex and the membrane. Numerical simulations predict that a blebbed profile is energetically favourable when membrane area exceeds the cortex area. However, this model does not account for volume conservation of cytosol. Further, the model does not include the possibility of membrane growth. Instead the cortex contracts and allows excess membrane to be released.

Whereas the above studies focus on the expansion phase of blebbing some groups have endeavoured to create systems that constantly evolve producing expansion and contraction. For example, Lim *et al.* (2012) developed an elastic sheet model that incorporates reattachment of the membrane to a substrate. By varying the rates of readhesion at either side of the bleb neck and including a time-dependent pressure, they were able to produce experimentally observed moving membrane waves known as ‘circus motion’ (Charras *et al.*, 2008).

Comparable with Strychalski & Guy (2012), Young & Mitran (2010) developed a numerical model, which includes interactions between intracellular fluids and membrane elastic structures. Their membrane model depends on a wave equation for the displacement, which was coupled to the pressure of the cytosol. In turn, the cytosol was governed by the Stokes equations. This formulation leads to numerous expansions and retractions of non-spherical protrusions.

Tozluoğlu *et al.* (2013) produced perhaps the most complete phenomenological model of membrane protrusions to date. They construct a hybrid model that couples viscoelastic finite-elements with sets of agents embedded in the membrane. The agents record the density of numerous important physiological quantities and thereby influence the properties of the viscoelastic connectors. Using this computational model, not only were the authors able to reproduce multiple different experimentally observed behaviours, but they also offer predictions as to how and why a cell might choose between lamellipodial and blebbing forms of motion.

Although, thus far, we have only considered blebs which are produced by the membrane (Funkhouser *et al.*, 2013) model an alternate form of blebbing, which occurs on the cell nucleus. Solution shapes are found using a Monte Carlo method to minimize the total elastic energy, which is the sum of bending and stretching energies. By altering the make up of the nucleus’ structure, the authors are able to account for large irregular nuclei shapes, which are thought to lead to pathological development.

1.3 Aim

In this paper, we review a previously developed axisymmetric elastic shell framework and its extension that includes reconfiguration of the reference state (Woolley *et al.*, 2014). In contrast to the above models that account for the fluid dynamics in the cytosol, we assume that the system relaxes on a very quick timescale, allowing us to step through adiabatic iterations and eliminating the need to explicitly consider the fluid dynamics of intracellular cytosol. Further, because the membrane–cortex adhesion proteins are very short we assume that the membrane and cortex can be treated as one compound shell.

The reconfiguring model was developed to ensure that the simulated membrane stretch remains less than 4%. However, although the reconfiguring system is biologically more accurate the corresponding simulations are comparatively slow. Thus, in order to speed up the simulations, but maintain small membrane stretches we develop a simpler third model by considering the semi-inverse problem of

constraining the original solid mechanical formulation to solutions that are only composed of spheres and spherical caps.

As long as we understand the validity of our assumptions then: the *stretch model*, which produces protrusions by stretching the compound shell; the *reconfiguring model* which produces protrusions by allowing the compound shell to grow and not just stretch and the *spherical model*, which fixes the shapes of the cell and bleb to be spheres, are each able to give useful predictions. Moreover, our goal is to compare all three blebbing descriptions and highlight which results are comparable across the models, thereby emphasizing the view that the complexity of the chosen mathematical framework should be consistent with the answers that are sought and the accessible data that the theory will be compared against.

We begin in Section 2 by briefly recapitulating the derivation of the stretch and the reconfiguration models. In Section 3, we solve the semi-inverse problem of the mechanical model under the assumption that bending can be ignored, thereby producing the spherical model. Further, we show numerically that within pertinent parameter regions this is the only stable solution to the semi-inverse problem. Similarities and differences between the stretch, reconfiguration and geometric models are presented in Section 5 and upon seeing that the geometric model is within experimental error for a number of results we extend this system and consider the case that two blebs are initialized in different configurations. Finally, in Section 6, we summarize the results, benefits and limitations of each model.

2. The mechanical model

Assuming that we can reduce the separate entities of the membrane and cortex to a single pressurized, axisymmetric elastic shell, which supports bending stresses, we adapt previous work on such shells (Evans & Skalak, 1980; Goriely & Tabor, 2003a,b, 2006; Goriely *et al.*, 2005; Tongen *et al.*, 2006). The nucleation of a shell protrusion is then realized by the reduction of the shell stiffness near the axis of rotational symmetry. An extended derivation of this blebbing model can be found in Woolley *et al.* (2014).

2.1 Kinematics

We define an orthonormal Euclidean basis, \mathbf{e}_x , \mathbf{e}_y and \mathbf{e}_z . Treating the z -axis as the axis of rotational symmetry, we construct a reference configuration, (z_{rc}, y_{rc}) , which corresponds to the unstressed state. This is the state in which the pressure difference across the membrane and the surface tension are zero. This reference configuration is parametrized by its arc length, σ , which is measured from the intercept of the curve with the z -axis (see Fig. 3).

In order to define the stressed solution state in the current configuration, we construct a new right-handed local basis, \mathbf{e}_s , \mathbf{e}_ϕ and \mathbf{n} , on the solution surface: \mathbf{e}_s is tangent to the solution curve and points in the direction of increasing σ ; \mathbf{n} is the outward pointing normal to the solution surface; \mathbf{e}_ϕ is perpendicular to both \mathbf{e}_s and \mathbf{n} , and points in the direction of increasing ϕ , where ϕ is the azimuthal angle around the axis of symmetry.

The exact form of the solution curve can be described through two variables, y and z , which are parametrized by the reference configuration's arc length. Here, $y(\sigma)$ is the distance between the surface and the z -axis along the \mathbf{e}_y direction and $z(\sigma)$ is the accompanying distance away from the origin along the z -axis (see Fig. 3). Further, we define $\theta(\sigma)$ to be the angle between the normal of the solution curve, $\mathbf{n}(\sigma, \phi)$, and the z -axis and, finally, $s(\sigma)$ is the arc length along the solution configuration.

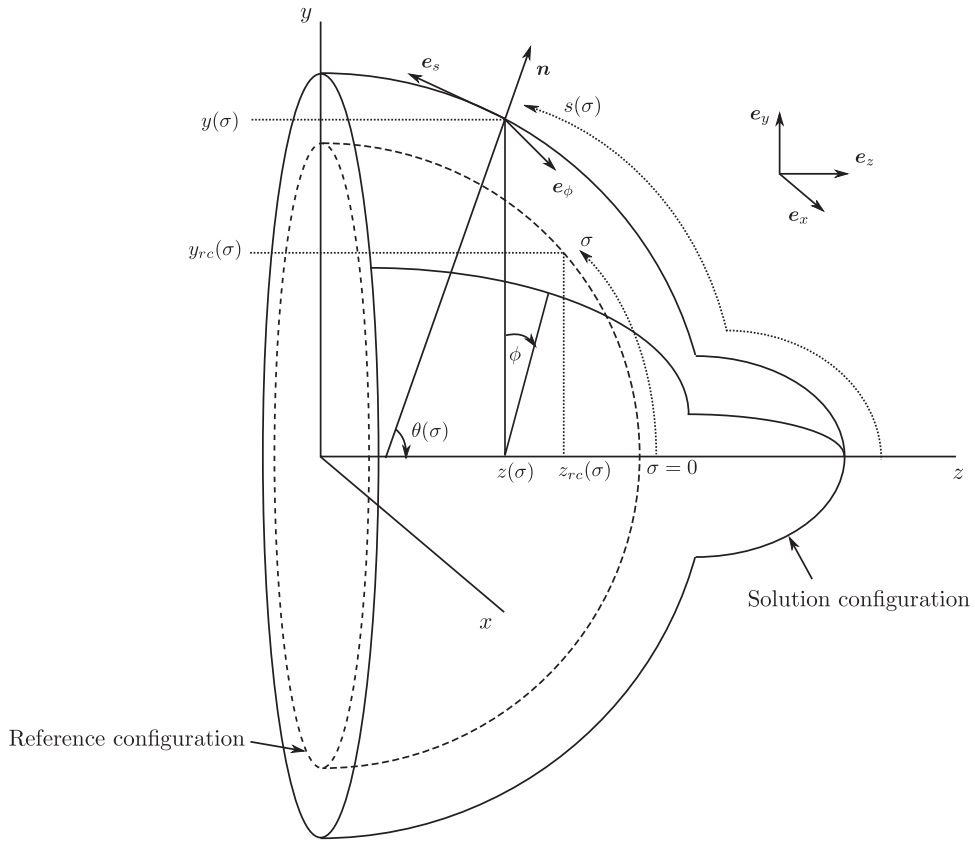


FIG. 3. The geometry of the reference and solution configurations.

The geometric variables, y and z , satisfy the following constraints:

$$\frac{\partial y}{\partial s} = \cos(\theta), \tag{2.1}$$

$$\frac{\partial z}{\partial s} = -\sin(\theta). \tag{2.2}$$

The reference and solution configurations are related via the following stretch ratios:

$$\lambda_\phi = \frac{y(\sigma)}{y_{rc}(\sigma)} \tag{2.3}$$

is the *radial stretch ratio*, which measures the axisymmetric deformation and

$$\lambda_s = \frac{\partial s}{\partial \sigma} \tag{2.4}$$

is the *arc length stretch ratio*, which measures the local stretching of the body coordinates with respect to arc length. Finally, the principal curvatures of an axisymmetric surface, κ_s and κ_ϕ , are defined as (Pressley, 2010)

$$\kappa_s = \frac{\partial\theta}{\partial s}, \quad (2.5)$$

$$\kappa_\phi = \frac{\sin(\theta)}{y}. \quad (2.6)$$

2.1.1 *Defining the reference configuration for the stretch and reconfiguring models.* Focusing on the application of the shell framework to cellular protrusions, we define the unstressed reference configuration to be a sphere, centred at the origin with radius ρ , thus $\sigma \in [0, \rho\pi]$ and

$$\lambda_\phi = \frac{y}{\rho \sin(\sigma/\rho)}. \quad (2.7)$$

Initially, in the stretch model, we assume that the reference configuration is fixed and all of the bleb deformation arises through stretching of the shell. In the reconfiguring model, we extend this framework to include reference configuration remodelling, meaning that the arc length and profile of the reference configuration are able to update according to some postulated evolution rule. Critically, we only remodel the reference configuration within the blebbing region $\sigma \in [0, \sigma_b]$, where σ_b denotes the maximum arc length of reference configuration that is weakened (Dai & Sheetz, 1999). This is biologically motivated by the fact that the non-blebbing cell surface has an intact cortex, and remodelling is determined by the dynamics of the actin network remodelling time scales much larger than those of membrane flow.

Appealing to experimental insights and using the fact that strains are small, we assume that the reference configuration relaxes linearly to the current membrane profile. Explicitly, if $y_{rc}(\Sigma, t)$ and $\Sigma = \Sigma(\sigma, t)$ are the profile of the reference configuration and corresponding arc length at time t , respectively, then

$$\frac{\partial y_{rc}}{\partial t}(\Sigma, t) = \eta(y(\Sigma, t) - y_{rc}(\Sigma, t)), \quad (2.8)$$

$$y_{rc}(\Sigma, 0) = \rho \sin(\sigma/\rho) \quad (2.9)$$

and

$$\frac{\partial \Sigma}{\partial t} = \eta(s - \Sigma), \quad (2.10)$$

$$\Sigma(\sigma, 0) = \sigma \in [0, \sigma_b]. \quad (2.11)$$

Note that in this reconfiguring case Σ also replaces σ in (2.3) and (2.4).

In order to apply the reconfiguration, the derivative form of the update rule is discretized, with each iteration defined to take Δt seconds. Due to the assumption that the solution is being progressed through adiabatic iterations, we must choose $\Delta t\eta$ to be small and $1/\eta$ to be larger than the viscous time scale, which is of the order 10^{-6} s (Sidell & Hazel, 1987). Consequently, a large number of iterations will be needed, meaning that reconfiguring simulations are slower than their non-reconfiguring counterparts, but are more closely aligned with the experimental observations.

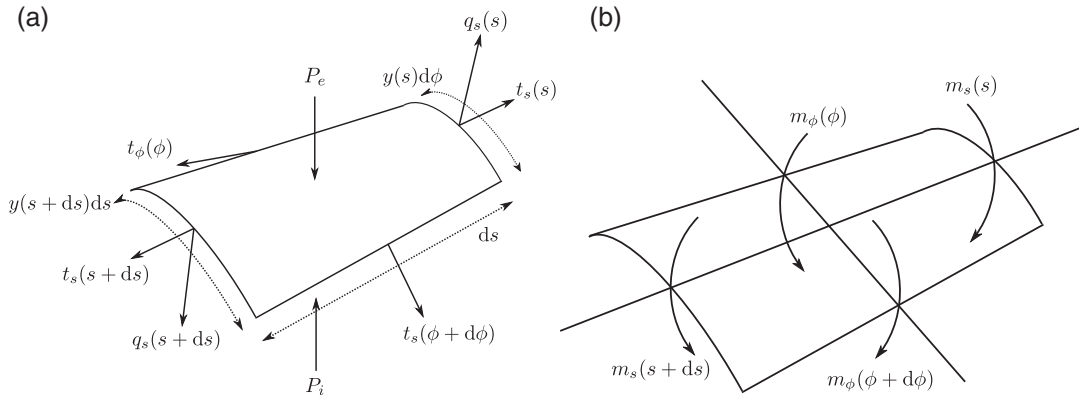


FIG. 4. Small section of the membrane on which: (a) the stresses and (b) the moments are defined.

2.2 Mechanics

Primarily, we are interested in the internal and external pressure, P_i and P_e , respectively, which act normally to the shell surface. Although the external pressure is assumed to be constant the internal pressure is used to enforce a constant volume constraint,

$$V = \left| \int_0^{\pi\rho} \pi y^2 \frac{\partial z}{\partial \sigma} \lambda_s \, d\sigma \right| = \int_0^{\pi\rho} \pi y(\sigma)^2 \lambda_s(\sigma) \sin(\theta(\sigma)) \, d\sigma. \tag{2.12}$$

Note, however, that the volume of the reference configuration in the reconfiguring model (and the geometric model discussed later) increases through the remodelling processes discussed in Section 2.1.1. Physically, this encapsulates the idea that cells are able to use blebs to rapidly produce more membrane locally and, thus, relieve the stretch felt by the cell.

In order to balance this pressure difference, the shell supports surface tensions, t_s and t_ϕ , that act along \mathbf{e}_s and \mathbf{e}_ϕ , respectively. Further, because we assume that the shell can support bending, there may be non-zero normal shear stresses, q_s , which act along \mathbf{n} , and non-zero moments, m_s and m_ϕ , about the \mathbf{e}_ϕ and \mathbf{e}_s axes, respectively, as illustrated in Fig. 4.

As we are approximating blebbing as an adiabatic process, the forces acting on the shell are in equilibrium. Defining $\Delta P = P_i - P_e$ and noting that $\partial t_\phi / \partial \phi = 0$ by axisymmetry, we derive the following normal and tangential force balances:

$$\frac{\partial q_s}{\partial \sigma} = \lambda_s \left(\Delta P - \kappa_\phi t_\phi - \kappa_s t_s - q_s \frac{\cos(\theta)}{y} \right), \tag{2.13}$$

$$\frac{\partial t_s}{\partial \sigma} = \lambda_s \left(\frac{\cos(\theta)}{y} (t_\phi - t_s) + \kappa_s q_s \right). \tag{2.14}$$

The moment balance equation is similarly constructed and leads to

$$\frac{\partial m_s}{\partial \sigma} = \lambda_s \left(\frac{\cos(\theta)}{y} (m_\phi - m_s) - q_s \right). \tag{2.15}$$

2.2.1 *Constitutive laws.* Although the theory in Sections 2.1 and 2.2 is valid for any constitutive law linking stresses and strains, we appeal to large deformation theory and specify the relationships to be

$$t_s = A(\lambda_s^2 + \mu\lambda_\phi^2 - (1 + \mu)), \quad (2.16)$$

$$t_\phi = A(\mu\lambda_s^2 + \lambda_\phi^2 - (1 + \mu)), \quad (2.17)$$

where A characterizes the elastic properties of the membrane and μ measures the relative extensibility of the membrane in the azimuthal and longitudinal directions (Skalak *et al.*, 1973; Evans & Skalak, 1980). Further, we assume that the bending moments are isotropic and proportional to the mean surface curvature, i.e.

$$m_\phi = m_s = M(\kappa_s + \kappa_\phi - K_0), \quad (2.18)$$

where K_0 is the mean curvature of the reference configuration and M is the bending modulus.

2.3 Integral condition

Currently, we have a system for seven variables ($y, z, \theta, s, q_s, t_s, \kappa_s$). This number can be reduced by using the quasi-static fluid hypothesis, meaning that pressure is spatially constant and, thus, we can derive an integral condition,

$$0 = \frac{\partial}{\partial s} \left(\Delta P \frac{y^2}{2} - \kappa_\phi y^2 t_s - q_s y \frac{\partial y}{\partial s} \right), \quad (2.19)$$

which stems from a horizontal force balance (Woolley *et al.*, 2014). The system can be further reduced by noticing that the equations for z and s , (2.2) and (2.4), respectively, decouple from the system, leaving only four equations in $(y, \theta, q_s, \kappa_s)$.

2.4 Boundary conditions for the stretch and reconfiguration models

We would like to apply the boundary conditions $y = 0$ and $\theta = 0$ at both $\sigma = 0$ and $\sigma = \pi\rho$ thereby providing four boundary conditions for four differential equations, leading to a correctly posed system. However, when $y = 0$ there is a singularity in the definition of the radial stretch ratio, (2.3), which is inherited in (2.13) and (2.15). In order to aid the convergence of the numerical solvers, we remove these singularities by reducing the solution domain to $\sigma \in [\epsilon, \pi\rho - \epsilon]$.

Beginning with the stretch model, we use regular power series expansions in the perturbation parameter ϵ to linearize the differential equations and use the leading order consistency equations as boundary conditions. Namely, if near $\sigma = 0$ we define $y(\epsilon) = y_1\epsilon$, $\theta(\epsilon) = \theta_1\epsilon$, $\kappa_s(\epsilon) = \kappa_{0s} + \kappa_{1s}\epsilon$ and $q_s(\epsilon) = q_{1s}\epsilon$ (where the zeroth order values of y , θ and q_s are fixed from the desired boundary conditions and (2.19)), then on substituting these into the differential system we find that $(y_1, \theta_1, \kappa_0, q_{1s})$ have to be solved for implicitly as part of the boundary value problem (BVP) through the equations

$$\theta_1^0 = \kappa_{s0}^0 y_1^0, \quad (2.20)$$

$$0 = \kappa_{s0}^0 (1 + \mu) A(0) (y_1^0)^3 - \left(\frac{\Delta P}{2} + \kappa_{s0}^0 A(0) (1 + \mu) \right) y_1^0 + q_{s1}^0, \quad (2.21)$$

where, by construction, y_1^0 is the root that connects continuously to the real, positive root that exists when, $q_{s1}^0 = 0$. The condition at $\sigma = \rho\pi - \epsilon$ is similar except: $\theta(\rho\pi - \epsilon) = \pi - \theta_1\epsilon$; the sign of the q_{s1} term in (2.21) is negative and we evaluate the stiffness parameter, A , at $\sigma = \pi\rho$, i.e. $A = A_+$.

The boundary conditions for the reconfiguring model are very similar. However, in the reconfiguring model we must also expand the reference configuration in terms of ϵ . Hence, if the reference configuration expansion has the form $y_{rc}(\epsilon) = \epsilon y_{rc1}^0$, then the boundary condition that replaces (2.21) is

$$0 = \kappa_{s0}^0 \frac{(1 + \mu(y_{rc1}^0)^2)A(0)}{(y_{rc1}^0)^2} (y_1^0)^3 - \left(\frac{\Delta P}{2} + \kappa_{s0}^0 A(0)(1 + \mu) \right) y_1^0 + q_{s1}^0, \tag{2.22}$$

with an equivalent condition at $\sigma = \rho\pi - \epsilon$.

3. Spherical model

As noted in much of the experimental literature (Cunningham, 1995; Charras *et al.*, 2008; Tinevez *et al.*, 2009), the shape of a bleb is an approximately spherical cap attached to an approximately spherical cell. This morphology has also been observed in the simulations of both the stretch and reconfiguring systems when the bending stiffness is made extremely small (Woolley *et al.*, 2014). Motivated by these observations, we consider the case in which the shell cannot support bending moments and solve a semi-inverse problem for the differential equations by constraining the reference configuration and solution geometry to be spherical as illustrated in Fig. 5.

This simplification depends on the definition of a piecewise smooth reference configuration that has been separated into a cell body and a blebbing part. By splitting the reference configuration in this way, we can, once again, focus on the remodelling of the blebbing section allowing us to form protrusions in a much simpler and quicker manner, whilst maintaining an area stretch of $<4\%$.

The reference and solution configuration each consist of two spheres. To specify the geometry, we define eight variables, $(\rho_c, \Theta_c, \rho_b, \Theta_b, r_c, \theta_c, r_b, \theta_b)$, where ρ_i and Θ_i are the radii and neck angles of the reference configuration and $i = c$ or b depending whether they are considered to be in the cell body or bleb, respectively. Similarly, r_i and θ_i are the solution variables (see Fig. 5). Having eight variables to define means that we need to specify eight independent governing equations. The first of these stems from volume conservation of the solution configuration,

$$V = \frac{4\pi R_0^3}{3} = \pi r_c^3 \left(\frac{2}{3} + \cos(\theta_c) - \frac{1}{3} \cos^3(\theta_c) \right) + \pi r_b^3 \left(\frac{2}{3} - \cos(\theta_b) + \frac{1}{3} \cos^3(\theta_b) \right), \tag{3.1}$$

where R_0 is the radius of the initial spherical solution.

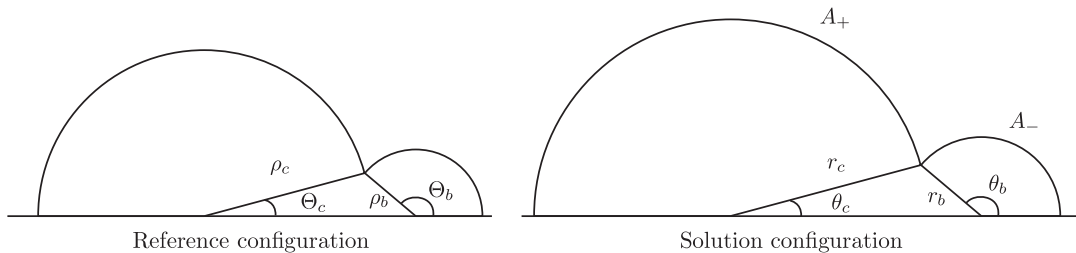


FIG. 5. Geometric variables defining a spherical model of blebbing.

In the absence of bending, $q_s = 0$, the system of shell equations reduces to

$$\frac{\partial y}{\partial \sigma} = \lambda_s \cos(\theta), \quad (3.2)$$

$$\frac{\partial z}{\partial \sigma} = -\lambda_s \sin(\theta), \quad (3.3)$$

$$\frac{\partial s}{\partial \sigma} = \lambda_s, \quad (3.4)$$

$$\frac{\partial \theta}{\partial \sigma} = \lambda_s \kappa_s, \quad (3.5)$$

$$\Delta P = \kappa_\phi t_\phi + \kappa_s t_s, \quad (3.6)$$

$$\Delta P = 2\kappa_\phi t_s, \quad (3.7)$$

where (3.7) arises from the first integral condition (2.19). Since we are assuming that the bleb and cell body parts are spherical caps, the curvatures are simply

$$\kappa_s = \kappa_\phi = \frac{1}{r}, \quad (3.8)$$

where

$$r = \begin{cases} r_b, & \sigma \leq \rho_b \Theta_b, \\ r_c, & \sigma > \rho_b \Theta_b. \end{cases} \quad (3.9)$$

Equations (3.6) and (3.7) can then be combined to show that $t_\phi = t_s$. From this, we derive

$$\lambda_s = \frac{y}{\rho \sin(\sigma/\rho)}, \quad (3.10)$$

where

$$\rho = \begin{cases} \rho_b, & \sigma \leq \rho_b \Theta_b, \\ \rho_c, & \sigma > \rho_b \Theta_b. \end{cases} \quad (3.11)$$

Substituting (3.10) into (3.2), we attain

$$\lambda_s \cos(\sigma/\rho) + \rho \frac{\partial \lambda_s}{\partial \sigma} \sin(\sigma/\rho) = \lambda_s \cos(\theta). \quad (3.12)$$

From the identity

$$\cos(\sigma/\rho + B) = \cos(\sigma/\rho) \cos(B) - \sin(\sigma/\rho) \sin(B), \quad (3.13)$$

we find that

$$\cos(\theta) = \cos(\sigma/\rho) + \frac{\rho}{\lambda_s} \frac{\partial \lambda_s}{\partial \sigma} \sin(\sigma/\rho) = \cos(\rho/\sigma + B), \quad (3.14)$$

where

$$\cos(B) = 1, \quad (3.15)$$

$$\sin(B) = -\frac{\rho}{\lambda_s} \frac{\partial \lambda_s}{\partial \sigma}. \quad (3.16)$$

Thus, $B = 2n\pi$ for $n \in \mathbb{Z}$, from which we choose $n = 0$. Also, this implies that

$$\frac{\partial \lambda_s}{\partial \sigma} = 0, \tag{3.17}$$

and so λ_s is a constant on both intervals of arc length. Using (3.5), we find that $\theta = \lambda_s \sigma / r$, where θ is defined as

$$\theta = \begin{cases} \theta_b, & \sigma \leq \rho_b \Theta_b, \\ \theta_c, & \sigma > \rho_b \Theta_b. \end{cases} \tag{3.18}$$

This, in conjunction with (3.10), produces

$$\lambda_s = \frac{r}{\rho}. \tag{3.19}$$

Moreover, we discover the condition that $\Theta_c = \theta_c$ and $\Theta_b = \theta_b$. Substituting this information into (3.2) and integrating across the discontinuity in the derivative between the cell body and bleb, we generate the expected continuity condition for the membrane solution,

$$r_c \sin(\theta_c) = r_b \sin(\theta_b). \tag{3.20}$$

The cell body and bleb coordinates are further linked by noting that the pressure is constant throughout the cell and, thus, appealing to (3.7),

$$[\kappa_\phi t_s]_{\text{bleb}} = [\kappa_\phi t_s]_{\text{cell body}}. \tag{3.21}$$

Using constitutive (2.16) for t_s , this can be simplified to

$$\frac{A_+}{r_c} \left(\left(\frac{r_c}{R_c} \right)^2 - 1 \right) = \frac{A_-}{r_b} \left(\left(\frac{r_b}{R_b} \right)^2 - 1 \right), \tag{3.22}$$

where A_+ and A_- are the stiffness parameters in the cell body and bleb, respectively, as defined in Section 2.2.1. Also note that once μ , ΔP and the initial reference configuration have been fixed R_0 can also be found using (2.16) and (3.7), i.e.

$$R_0 = \frac{\Delta P \rho^2}{4A_+(1 + \mu)} + \frac{1}{2} \sqrt{\left(\frac{\Delta P \rho^2}{2A_+(1 + \mu)} \right)^2 + 4}. \tag{3.23}$$

Having derived equations (3.1), (3.20), (3.22) and the two equalities linking the reference and solution angles, we have produced five algebraic equations for eight unknowns, leaving three degrees of freedom left to constrain. One of these will be used to update the reference configuration at each iteration. For consistency, we specify the update rule to be analogous to (2.10) and (2.11). Finally, the last two algebraic constraints stem from the assumption that the cell body does not change throughout the blebbing cycle and, so, the ρ_c and Θ_c are fixed to be constants. In summary, the algebraic conditions we

wish to satisfy are:

$$r_c \sin(\theta_c) = r_b \sin(\theta_b), \quad (3.24)$$

$$\frac{A_+}{r_c} \left(\left(\frac{r_c}{\rho_c} \right)^2 - 1 \right) = \frac{A_-}{r_b} \left(\left(\frac{r_b}{\rho_b} \right)^2 - 1 \right), \quad (3.25)$$

$$\theta_b = \Theta_b, \quad (3.26)$$

$$\theta_c = \Theta_c, \quad (3.27)$$

$$V = \pi r_c^3 \left(\frac{2}{3} + \cos(\theta_c) - \frac{1}{3} \cos^3(\theta_c) \right) + \pi r_b^3 \left(\frac{2}{3} - \cos(\theta_b) + \frac{1}{3} \cos^3(\theta_b) \right), \quad (3.28)$$

$$\Theta_c = \text{Constant}, \quad (3.29)$$

$$\rho_c = \text{Constant}, \quad (3.30)$$

$$\frac{\partial \sigma_b}{\partial t} = \eta(s(\sigma_b) - \sigma_b), \quad (3.31)$$

where (3.24–3.27) are required to ensure that the spherical model is a solution of the differential equation system (3.2–3.7) and (3.28–3.31) are chosen based on experimental observations (Collins-Hooper *et al.*, 2012).

3.1 Extension to two blebs

Due to the spherical model's simplicity, we are able to extend the framework to consider multiple blebs; at either end of the cell, or on top of each other. Cells with multiple blebs are frequently observed and can be experimentally initiated in such specific places using laser ablation of the cortex (Tinevez *et al.*, 2009). Concordantly, we add a further sphere on to the reference configuration at either the $\sigma = 0$ end (the bleb-on-bleb case) or the $\sigma = \rho_c(\pi - \theta_c) + \rho_b\theta_b$ end (opposite-bleb case). The extra sphere modelling the solution configuration is then added analogously (see Fig. 6).

Although not explicitly derived here the equations for the two bleb cases shown in Fig. 6 are simple extensions of (3.24–3.31). Explicitly, the reference configuration bleb variables in the one bleb case are renamed to become (ρ_{b1}, Θ_{b1}) and additional variables are included to account for the second bleb (ρ_{b2}, Θ_{b2}) . Solution configuration variables are included in an analogous way. Moreover, once we have specified the second bleb's neck angle, Θ_{2c} , continuity equations, pressure balances, volume constraints and update rules controlling the bleb arc length can all be derived as in the single bleb case, leading to a complete and consistent set of algebraic equations. Note that in order to aid comparisons between the simulations, we specify that both blebs are initialized over the same angle, i.e. $\Theta_{1c} = \Theta_{2c}$. This constraint is easily relaxed and has minimal effects on the resulting conclusions.

3.2 Stability of the spherical solution

It is well known that general existence and uniqueness proofs do not exist for BVPs. Further, it is often the case that such proofs are not possible as there are simple examples of linear differential equations, which, when solved as a BVP, offer no solution, or perhaps even multiple solutions (Bernfeld & Lakshminantham, 1974). Having solved the semi-inverse problem, we see that existence is not an issue; thus, in this section we appeal to linear analysis and numerical techniques to show that in the case where A is

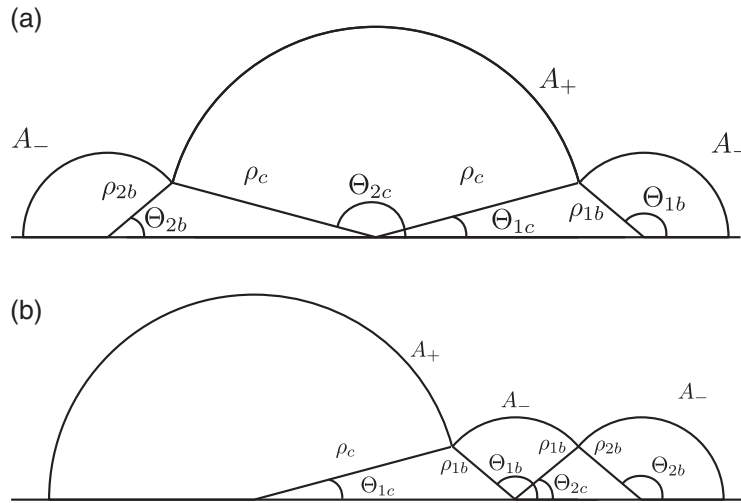


FIG. 6. Schematic diagrams for the case that two blebs are nucleated: (a) at opposite ends of the cell and (b) on top of one another.

constant over the reference configuration no sufficiently small perturbation of the spherical solution can also be a solution of the BVP (3.2–3.7). Hence, in finding the spherical solution, any such perturbations must dissipate.

We begin by repeating that (3.3) and (3.4) decouple leading to a simplified system. Further, by appealing to the definitions of κ_ϕ and the constitutive equation of t_ϕ in (2.6) and (2.17) we are able to dramatically simplify system (3.2–3.7) to

$$\frac{\partial y}{\partial \sigma} = \lambda_s \cos(\theta), \tag{3.32}$$

$$\frac{\partial \theta}{\partial \sigma} = \frac{2\lambda_s}{y} \sin(\theta) - \frac{A\lambda_s}{\Delta P} \sin(\theta)^2 \left(\frac{(\mu \lambda_s^2 - 1 - \mu)}{y^2} + \frac{1}{\rho^2 \sin(\sigma/\rho)^2} \right), \tag{3.33}$$

$$\lambda_s^2 = \frac{\Delta P y}{2 \sin(\theta) A} - \mu \left(\frac{y}{\rho \sin(\sigma/\rho)} \right)^2 + 1 + \mu. \tag{3.34}$$

Upon substituting

$$y = r \sin \left(\frac{\sigma}{\rho} \right) + f_1(\sigma), \tag{3.35}$$

$$\theta = \frac{\sigma}{\rho} + f_2(\sigma), \tag{3.36}$$

into (3.32–3.34) and linearizing about $f_1 = f_2 = 0$ we derive

$$\frac{df_1}{d\sigma} = -\frac{\cos(\sigma/\rho)(r^2(\mu - 1) + \rho^2(1 + \mu))}{2\rho r^2 \sin(\sigma/\rho)} f_1 - \frac{(r^2(\mu - 1) - \rho^2(1 + \mu)) \cos(\sigma/\rho)^2 + 2r^2}{2\rho r \sin(\sigma/\rho)} f_2, \tag{3.37}$$

$$\frac{df_2}{d\sigma} = \frac{(r^2 + \rho^2 t)(r^2(\mu - 3) + \rho^2(1 + \mu))}{2\rho r^3 \sin(\sigma/\rho)(r^2 - \rho^2)} f_1 + \frac{\cos(\sigma/\rho)(r^2(\mu - 1) + \rho^2(1 + \mu))}{2\rho r^2 \sin(\sigma/\rho)} f_2. \quad (3.38)$$

We consider the linearized equations on the interval $\sigma \in [\epsilon, \rho_c \pi - \epsilon]$. Because we are demanding spherical symmetry then on the cell body, we impose the following boundary conditions:

$$f_1(\epsilon) = f_1(\rho_c \pi - \epsilon), \quad (3.39)$$

$$f_2(\epsilon) = f_2(\rho_c \pi - \epsilon), \quad (3.40)$$

with analogous conditions being defined at the end points of the bleb's arc length. In order to see that the only possible solution that exists for this BVP is the trivial solution $(f_1(\sigma), f_2(\sigma)) = (0, 0)$, consider two solutions, $(f_1^1(\sigma), f_2^1(\sigma))$ and $(f_1^2(\sigma), f_2^2(\sigma))$, with linearly independent initial condition, e.g. $(f_1^1(\epsilon), f_2^1(\epsilon)) = (1, 0)$ and $(f_1^2(\epsilon), f_2^2(\epsilon)) = (0, 1)$. Further, suppose that for some initial condition a solution satisfying (3.37) and (3.38) and boundary conditions (3.39) and (3.40) exists. We can then write this specific initial condition as a linear combinations of the linearly independent solutions and, so, for some α and β ,

$$\alpha \begin{bmatrix} 1 \\ 0 \end{bmatrix} + \beta \begin{bmatrix} 0 \\ 1 \end{bmatrix} = \alpha \begin{bmatrix} f_1^1(\rho_c \pi - \epsilon) \\ f_2^1(\rho_c \pi - \epsilon) \end{bmatrix} + \beta \begin{bmatrix} f_1^2(\rho_c \pi - \epsilon) \\ f_2^2(\rho_c \pi - \epsilon) \end{bmatrix}. \quad (3.41)$$

In order for a non-zero solution to exist, we must have that the determinant of

$$\begin{bmatrix} f_1^1(\rho_c \pi - \epsilon) - 1 & f_1^2(\rho_c \pi - \epsilon) \\ f_2^1(\rho_c \pi - \epsilon) & f_2^2(\rho_c \pi - \epsilon) - 1 \end{bmatrix} \quad (3.42)$$

is zero.

Unfortunately, we are unable to evaluate the entries of matrix (3.42) analytically, thus, we must turn to numerical evaluations. Fixing $\epsilon = 10^{-6}$ then for one hundred linear spaced evaluations within the parameter regions $0.2 < \mu < 0.99$, $1 < \rho < 5$ and $5.028 < r < 6$ only the trivial solution $(\alpha, \beta) = (0, 0)$ exists (data not shown). Thus, at least for the given ranges, the spherical solution is stable with respect to other spherically symmetric solutions. Note that there has been some recent work suggesting that pear shape instabilities may be possible (Goriely, 2013).

4. Iteration methods

We now return to the mechanical models and discuss the method through which protrusions are produced. Blebs are produced in the stretch model through reducing the stiffness parameter A near $\sigma = 0$ causing preferential stretching to occur within this region. Specifically, in the stretch and reconfiguration models we specify a tanh profile of the form

$$A(\sigma) = A_+ \left(1 + \frac{1}{2} \left(1 - \frac{A_-}{A_+} \right) (\tanh((\sigma - \sigma_b)\beta) - 1) \right), \quad (4.1)$$

where A_+ and A_- determine the stiffness of the shell away from, and close to, the bleb region, respectively (see Fig. 5). The parameter σ_b controls the arc length of shell that is weakened and $1/\beta$ defines the length scale over which weakening occurs. Because the adhesion proteins that link the membrane and the cortex are very small, we expect β to be large causing the transition between stiff, fully adhered

membrane–cortex shell to softer, delaminated membrane to occur over a very small spatial scale. Thus, throughout all the simulations we use $\beta = 20 \mu\text{m}^{-1}$. In the geometric sphere model, the parameter A is defined piecewise, i.e. $A = A_+$ on the cell body sphere and $A = A_-$ on the bleb sphere, thus mimicking the sharp transition of the tanh function in (4.1).

The stretch, reconfiguration and spherical model simulations each begin with 10 iterations that reduce A in the bleb region. This corresponds to the extremely quick delamination process. This weakening continues only in the stretch model, which relies on the reduction of A in order to produce sizeable protrusions. In particular, A is reduced in the bleb region until the blebs in the stretch model extend to $1.5 \mu\text{m}$, which is the order of size that we are considering (Otto *et al.*, 2011; Collins-Hooper *et al.*, 2012). Although, as previously stated, the stretch model will cause the shell to stretch further than the accepted figure of 4%, we use it as a simple proxy mechanism through which protrusions can be formed. Later, in Section 5, we will see that many results of the stretching model are similar to the more realistic reconfiguration model.

In the reconfiguration and spherical simulations, the membrane is not further weakened after these ten iterations. Instead, once the minimum value of A_- is achieved the weakening iterations are stopped and the reference reconfiguration is activated. Thus, in each iteration the equilibrium configuration is simulated, the reference configuration is updated through (2.8) and (2.10), and the iteration begins again. In these cases, the minimum value of A_- is chosen to ensure that the area increase of the stretch model is close to, but no greater than, 4% after the first 10 iterations. In the present case, $A_- = 368 \text{ pN}/\mu\text{m}$, which produces a maximum area increase of 3.9% in the reconfiguration model.

5. Results

One of the primary simulated results of interest is the cell profile and, so, in a number of figures, extension of the bleb is used as a measure of cell deformation. The extension is important when considering bleb-based motility, as it has been shown that such motion is greatly retarded if blebs are too small, or too big (Otto *et al.*, 2011). Bleb extension is calculated by subtracting the diameter of the cell body from the maximum width of the weakened cell, see Fig. 7. Later, when we consider two blebs, we use the sum of the extensions of each bleb.

In Fig. 8, we plot the blebbed profiles for each of the three models discussed in the previous sections, namely the mechanically derived shell system (stretch model) that creates protrusions through stretching the reference configuration (Section 2.1), its extension (reconfiguration model) that depends on reference configuration evolution to produce membrane protrusions (Section 2.1.1) and the simplified geometric description (spherical model) that also requires the reference configuration to be remodelled for blebs to appear (Section 3). Note that throughout this section, we only allow the blebs to extend to a maximum of $1.5 \mu\text{m}$, which is an average size for the satellite stem cells that we are particularly interested in (Otto *et al.*, 2011; Collins-Hooper *et al.*, 2012). Theoretically, we have much more freedom, suggesting that this framework is very flexible and is applicable to cells and blebs of various sizes.

Critically, the spherical model only satisfies the semi-inverse problem when the bending stiffness $M = 0$. Fortunately, although a cell's membrane bending stiffness is non-zero, it is still very small, $M = 10^{-2} \text{ pN } \mu\text{m}$, when compared with the shell stiffness, $A = 10^2 - 10^3 \text{ pN}/\mu\text{m}$ (Keller & Egli, 1998; Dai & Sheetz, 1999; Pozrikidis, 2001; Collins-Hooper *et al.*, 2012), meaning that the spherical model is a close match to its geometrically unconstrained analogues. The fact that the reconfiguration and the spherical models match so well may not be so surprising because the shell is weakened to same amount and it is the reference configuration evolution that drives the protrusion. However, it is of interest to

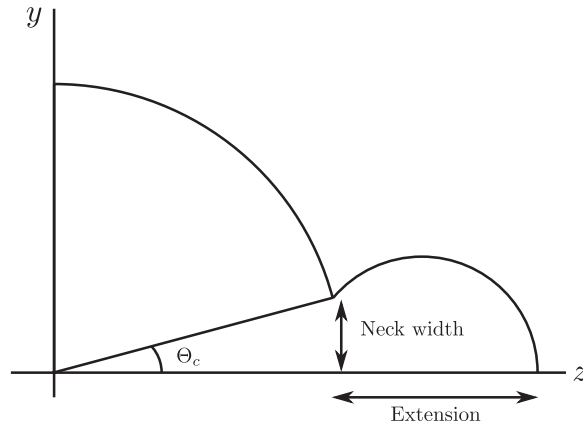


FIG. 7. Illustrating important measures of bleb size. θ_c is the angle which controls how much of the original membrane is weakened. In the stretching and reconfiguring models, the neck width, $y(\theta_c)$, must be calculated. In the spherical model, it has the explicit form $r_c \sin(\theta_c)$.

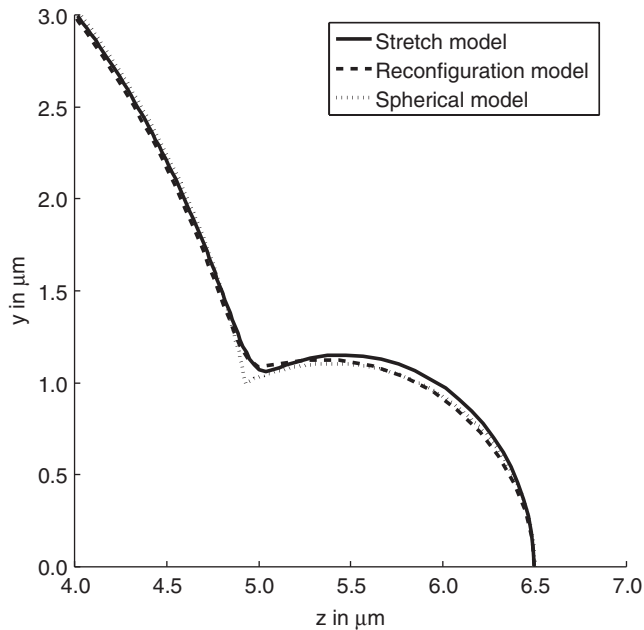


FIG. 8. The blebbed profile of the spherical model compared against the profiles of the stretch and reconfiguration models. The cell body is centred at the origin. Parameters are $\rho = 5$, $A_+ = 10^3$ pN/ μm , $\theta_c = \frac{1}{5}$, $\mu = 0.5$, $M = 10^{-2}$ pN μm and the initial pressure difference was $\Delta P = 10$ Pa. In the stretch case, the membrane stiffness in the bleb was reduced to $A_- = 0.58$ pN/ μm . In the reconfiguration and spherical cases, the membrane stiffness in the bleb was reduced to $A_- = 368$ pN/ μm . Each simulation was run until the blebbed membrane extended to 6.5 μm .

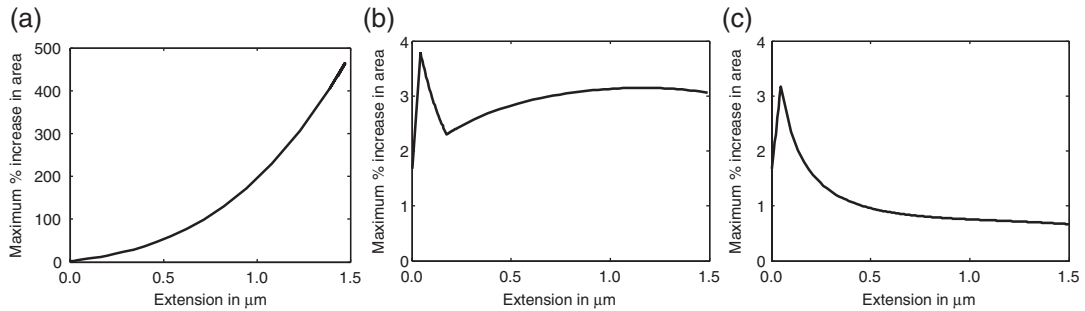


FIG. 9. Comparing the maximum increase in area of the: (a) stretching model; (b) reconfiguration model and (c) spherical model. Parameters are as in Fig. 8.

observe that the reconfiguration model profile matches the stretching model profile so well, even though the underlying process that produces the extension is fundamentally different. Critically, although the spherical model is closer to the reconfiguration model all three profiles are well within experimental error of each other, which is around 10%.

The biggest difference between these three models can be seen in Fig. 9 which illustrates how much the membrane stretches as the bleb is formed. The maximum increase in area is calculated as a percentage increase over the reference state area through the product of the azimuthal and arc length stretches,

$$\max_{\sigma} 100(\lambda_s \lambda_{\phi} - 1). \quad (5.1)$$

As expected the stretch model soon violates the maximum 4% increase in area, which would lead to membrane tearing. This can be compared with the reconfiguration and spherical models that clearly stay below 4%. The area stretch in Fig. 9(a,b) initially rises as the extension is being driven purely by weakening since A_- is being reduced to its minimum value with no evolution of the reference configuration during these first 10 iterations.

After the peak in area stretch, both reconfiguration and spherical cases see a rapid drop in the area stretch as the reference configuration begins to catch up with the solution configuration. In the spherical case, this is all that occurs and, so, as the extension increases the pressure in the cell reduces to maintain the volume constraint. As the pressure reduces the difference between the solution and reference configurations reduces, as illustrated by Fig. 9(c). This can be compared with the reconfiguration model in Fig. 9(b) that does not undergo a monotonic decrease. The reason behind the second increase is that due to having non-zero bending moments a neck region starts to form that smoothly transitions from the stiff cell body membrane to the weaker bleb membrane. Critically, the increased departure of the solution from the reference state causes the area stretch to increase because the cell body reference configuration is not updated. However, similar to the spherical model, as the bleb extends the pressure difference drops, thus, as the extension of the bleb reaches approximately 1.3 μm the neck region stops moving away from the cell body reference configuration and instead the drop in pressure brings the neck region closer to the reference configuration, thereby causing a second reduction in area stretch. Although the spherical model is unable to capture this non-monotonic behaviour, the main conclusion we reach is that by reconfiguring the reference state the membrane area increase is $<4\%$. Note that each of the bleb membranes that we produce constitute $<10\%$ of the entire surface area of the original cell

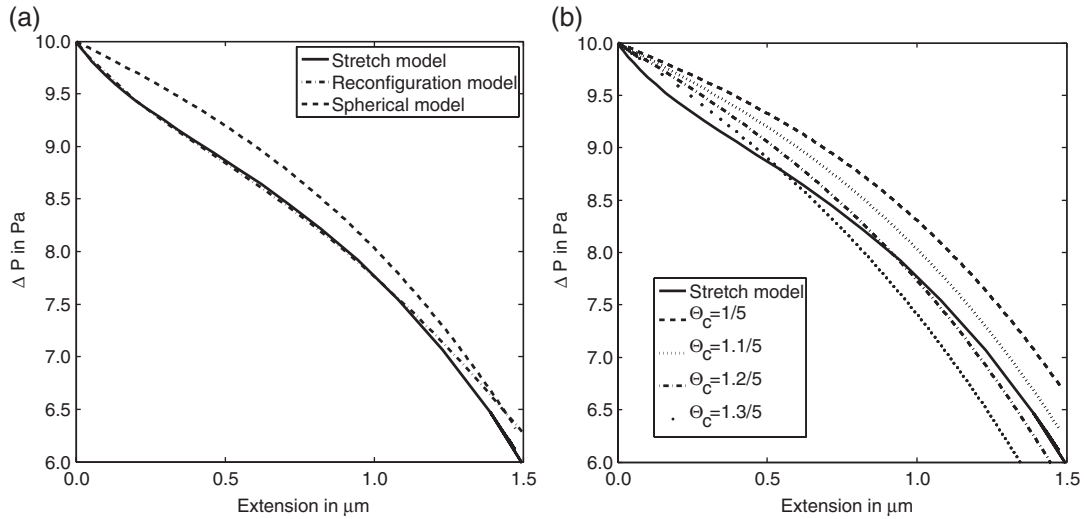


FIG. 10. (a) Comparing the pressure difference between the stretching, reconfiguration model and spherical model. (b) Comparing the pressure difference between the stretching model and the spherical model as the weakening angle, Θ_c , is increased in the spherical model. Unless otherwise stated in the figure, the parameters are as in Fig. 8.

and, thus, we are well within the limits of membrane that can be rapidly produced by unwrinkling and exocytosis, as discussed in Section 1.

Another key measure is the relationship between pressure change and bleb size. Figure 10(a) illustrates that the pressure within both the stretch and reconfiguration models are very similar, although they do start to diverge as the bleb becomes larger. This was considered further in Woolley *et al.* (2014) where it was discovered that the reconfiguration model can produce blebs with a larger extension with the same initial pressure difference. Fortunately, these bleb sizes are outside the physical range that we observe in satellite muscle stem cells and, thus, this divergence is of no concern (Otto *et al.*, 2011; Collins-Hooper *et al.*, 2012).

If we compare the evolution of the pressure differences for both the mechanical models and the spherical model, we see that they are qualitatively the same with a monotonically decreasing trend as the bleb extends. Quantitatively, for a given bleb extension $< 1.5 \mu\text{m}$ the spherical model's pressure difference is 0.5–1 Pa, or 5–10% larger than those of the mechanical models. This discrepancy arises due to the static neck region in the spherical model. By considering Fig. 8, we see that the biggest deviation of the models occurs in the neck region. In the stretching and reconfiguration models, the small, but non-zero, bending causes the cell profiles to have a smooth transition between the bleb and cell body, leading to a slightly larger neck width and, thus, a slightly larger bleb. Due to conservation of volume and blebs acting to reduce the pressure difference (Fig. 10(a)), the larger blebs in the stretching and reconfiguration models cause these two mechanical models to have a lower pressure difference than the spherical model. This is evidenced by Fig. 10(b), which demonstrates that if the neck angle of the spherical model, Θ_c , is slightly increased the pressure difference drops accordingly. From Fig. 10(b), we can use the spherical models to estimate that the final neck width of the mechanical models is in the range $[r_c \sin(1.1/5), r_c \sin(1.2/5)] \approx [1.1, 1.2] \mu\text{m}$, which matches the neck width seen in Fig. 8. Critically, although we have presented the source for this small quantitative difference between the

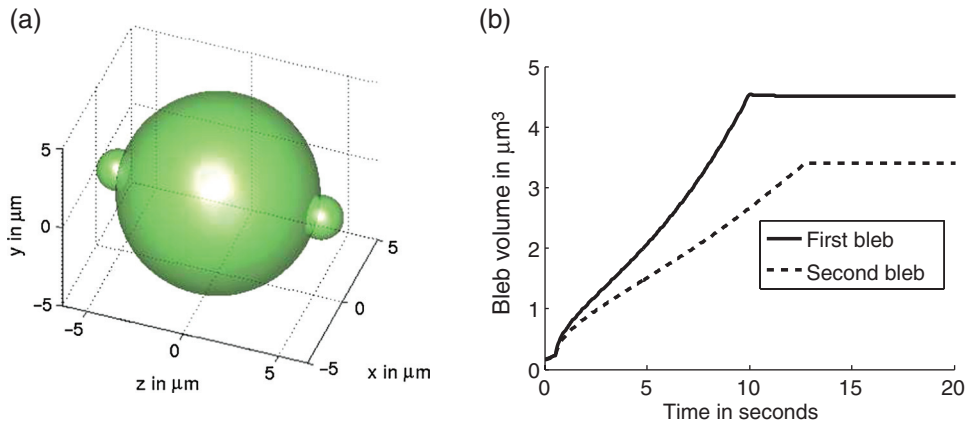


FIG. 11. (a) 3D structure of blebs nucleating at opposite ends of a cell body. The view has been made slightly transparent, in order that we may be able to see the connection of the furthest bleb. (b) Comparing the speed at which the two blebs form in terms of how quickly the volume increases. Parameters are as in Fig. 8 with the addition of $\theta_{2c} = \pi - \frac{1}{5}$.

mechanical and spherical models the observed difference is within standard experimental errors, which is around 10%. Thus, we conclude that the spherical model is suitable for blebs that extend $< 1.5 \mu\text{m}$.

5.1 Two bleb nucleation

Having demonstrated the equivalence between the mechanical and spherical simulations to within observational errors, we use the spherical model's simple nature to explore the morphologies obtained by nucleating a second bleb. Our first extension considers the possibility of nucleating two blebs at opposite ends of the bleb body akin to the laser cortex ablation experiments done by *Tinevez et al. (2009)*. In Fig. 11(a), we see the 3D shape of the membrane–cortex compound shell. Here we assume that bleb initialization is identical at both the front and the back and so the bleb necks are the same width.

In order to compare the speed of formation of the two blebs, we need to fix the time scale, $\eta\Delta t$ (discussed in Section 2.1.1), which is assumed to be constant throughout the simulation. In particular, this time scale is chosen to ensure that the first bleb takes 10 s to reach an extension of $1.5 \mu\text{m}$, which is a typical time that is found in the literature. The product $\eta\Delta t$ measures how quickly a cell can produce extra membrane and we assume it is intrinsic to the cell and is fixed for all blebs. This is justifiable as a cell has the ability to produce large amounts of membrane (potentially more than 50% extra) before it begins to encounter problems (*Hallett et al., 2008*), thus the rate at which membrane can be created for one bleb does not affect the formation of the second. However, blebs do not grow at the same rate as the update rule is also proportional to the difference between the solution and reference configuration arc lengths, see (2.10). Upon fixing $\eta\Delta t$, the second bleb is allowed to grow until it is $\frac{3}{4}$ of the volume of the first bleb. This reduction in volume of a second bleb was discovered by *Tinevez et al. (2009)*.

Using these data, we are able to compare the bleb growth rates in Fig. 11(b). Clearly, the growth rate of the second bleb is slower than the first. This is understandable because our update rule is proportional to the difference between the reference and solution arc lengths and as the first bleb grows at the front the pressure drops, causing the cell body solution radius to decrease slightly. Thus, when it comes to the initiation of the second bleb the difference in arc length between the second bleb and the process of reference configuration is much smaller, resulting in a slower growth rate. Hence, we recover the

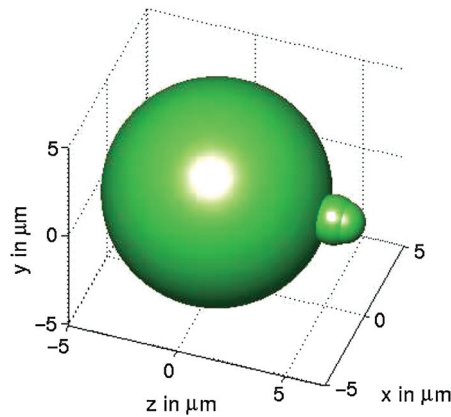


FIG. 12. 3D structure of blebs nucleating on top of each other. Parameters are as in Fig. 8 with the addition of $\theta_{2c} = \theta_{b1}$.

experimental result that while the second bleb's volume is smaller its growth rate is small enough to ensure that its growth phase lasts longer (Cunningham, 1995).

The second extension we consider involves the construction of a bleb on top of a preformed bleb (see Fig. 12). Such protrusions, which have been called lobopodia, are observed to occur biologically. It is thought that these new blebs could form in one of two ways. First, they could form like any other normal bleb, such that once the bleb growth has stopped and the actin cortex has reformed then the membrane delaminates from the cortex again (see Fig. 2). Secondly, it is possible that the reformed cortex is weaker than the rest of the cell's cortex, causing this to be the site of preferential blebbing (Yoshida & Soldati, 2006; Charras & Paluch, 2008). In our simulations, we consider the former case and nucleate the second bleb on top of the first, only after the first is stabilized. Explicitly, after the first bleb has been allowed to grow for 10 s the reconfiguration process stops acting over the entire bleb and continues only over the reduced arc length, $s = \rho_{1b}\theta_{2c}$, see Fig. 6.

Since we are able to generate elongated blebs and, thus, generalize our analysis to non-spherical protrusions, we can compare the extensions and pressure relationships in the bleb-on-bleb case with the opposite-bleb model discussed previously. In order to compare the simulation, we use the same time scale (derived from the opposite-bleb case) in both simulations and compare the same amount of physical time, i.e. 20 s.

As we might expect the opposite-bleb case is able to produce a cell that can extend much further than the bleb-on-bleb case, which is illustrated in Fig. 13(a). This makes sense because by building on the first bleb, the cell is not using the first bleb's full extension. Also note that until 10 s the graphs of each case lie on top of each other because the first bleb is initialized in exactly the same way in both cases. Beyond 10 s we observe that not only does the opposite-bleb case extend further, but it does so at a quicker rate, which can be seen as the solid and dashed lines begin to diverge.

Note that since pressure is spatially uniform, we would be unable to use pressure to visualize the evolution differences between the first and second blebs. Alternatively, we consider surface tensions of the blebs and cell body, which are proportional to the solution radii multiplied by the pressure. Thus, not only do we maintain a measure of the pressure, but we are also able to illustrate the different evolutions of the surface tension in the cell body and blebs, as seen in Fig. 13(b,c). Note that, although the final surface tensions in both blebs and across both treatments are approximately the same, the cell body's

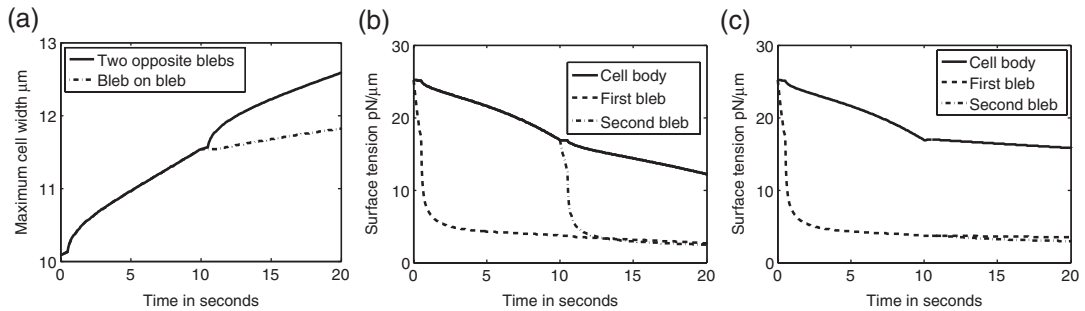


FIG. 13. Comparing two-bleb scenarios. (a) Maximum width of the cell over time in both cases of opposite-bleb and bleb-on-bleb formation. Parameters are the same as in Figs 11 and 12, respectively. (b) Surface tension of the cell body and two blebs in the opposite-bleb formation case. Parameters are the same as in Fig. 11. (c) Surface tension of the cell body and two blebs in the bleb-on-bleb formation case. Parameters are the same as in Fig. 12. In all cases, the second bleb is initiated 10 s after the first bleb.

surface tension demonstrates higher variability. This difference in the cell body's surface tension stems from the extensions in the opposite-bleb case being larger, this causes the pressure to drop further in the cell body in order to maintain constant volume. This means that as the second bleb forms in the bleb-on-bleb case the pressure and the cell body radius are larger, causing the surface tension in the cell body to be larger because of Laplace's law.

6. Conclusion

Cells are able to produce multiple different types of membrane protrusions such as lamellipodia, filopodia and lobopodia (Bukoreshtliev *et al.*, 2013). We have focused on a specific variety, known as blebs, that are driven by a pressure difference across the membrane. Blebs are used for multiple purposes, including locomotion. In this paper, we have compared a mechanical membrane stretching model (stretch model), an extended form, which includes reference reconfiguration (reconfiguration model) and a simplified spherical model (geometric model) that also includes reference state remodelling. Our aim is to illustrate that all three models are able to offer insights within certain regions of validity. Critically, although the models exhibit a hierarchy of physical detail, they also form a hierarchy of simulation difficulty and, thus, our choice of description must not simply depend on which is closest to reality, but also the suitability of the model to address our modelling needs, in terms of reproducing available experimental data.

The first result, illustrated in Fig. 8, shows that the protruded morphologies of all three models are very similar, thus, justifying the blebbing literature's liberal use of fitting spheres to blebs (Cunningham, 1995; Dai & Sheetz, 1999; Tinevez *et al.*, 2009). Further, it also justifies a number of mathematical membrane models that ignore bending stiffness altogether, as not only is the membrane bending stiffness small, but it only has a significant effect when the curvature of the surface becomes large, i.e. in the neck region.

The results concerning pressure difference evolution, Fig. 10, add further weight to the conclusion that the models are very similar, as all three models have similar monotonic decreasing relationships between the bleb extension and the pressure difference. The main source of discrepancy has been seen to be the spherical model's explicit definition of the neck region; a smaller neck width causes the spherical model to over estimate the pressure difference. This means that the spherical model is particularly valid if the neck size data are freely available, or if an average value can be estimated.

Although the profiles and pressures are very similar the amount the area stretches within each model is very different, Fig. 9. As cellular membrane is only able to support a 4% increase in area before lysis occurs (Nichol & Hutter, 1996; Dai & Sheetz, 1999; Sheetz *et al.*, 2006) this confirms the need for a source of membrane growth. Hence, the stretching model should only be used in the case that accurate measures of membrane growth are not needed, but definite information on the pressure difference is desired. In the spherical and reconfiguration models, we are always able to maintain an area stretch of <4%. However, even between these two descriptions the evolution of the increase in area is different as the reconfiguration model includes factors such as membrane moving away from the reference state and increasing the bleb's neck width. This movement is experimentally observable as a peeling of the membrane away from the cortex. In contrast, because of the piecewise nature of the spherical model, a neck width increase is not currently considered in this scenario. However, the model could be extended to include such an action depending on the assumption of a suitable constitutive relation that would open the bleb's neck as it grows. This is an area of potential future development.

We then extended our axisymmetric framework to consider cells with two blebs, either placed diametrically opposite about the axis of spherical symmetry (opposite-bleb case) or nucleated on top of one another (bleb-on-bleb case). This led us to produce two emergent results concerning the time over which the bleb takes to form and how much the surface tension is reduced through the blebs. In the opposite-bleb case, Fig. 11 shows that it will take longer for the second bleb to form, even though it grows to only three quarters of the size of the first. This result depends completely on the balance of the growth rate and volume size. It could have been the case that although the growth rate was reduced it was only reduced by a small amount and, thus, it would be able to create a second smaller bleb in a quicker time than 10 s. Using our results, we are able to suggest an explanation for why small blebs take longer to form, which has been observed by Cunningham (1995); once large blebs are created smaller blebs must be produced because the pressure difference has been lowered significantly. This lower pressure causes the reference and the solution configurations to be closer, which causes the reference configuration to remodel slower, since the update rule is postulated to be proportional to the difference between the reference and solution arc lengths.

Our second result pertains to the fact that a cell that blebs at opposite ends will grow wider more quickly than if a bleb is nucleated on top of another, Fig. 13(a). This causes the pressure and hence surface tension to drop quicker in the opposite-bleb case when compared with the bleb-on-bleb case, Fig. 13. We conclude that if a cell is in the process of reducing its pressure difference, it is more likely to create distinct blebs, rather than nucleate blebs on top of blebs. Blebs nucleating on blebs are more likely to stem from regions where the reformed actin cortex is weaker or cortex–membrane adhesions are in lower concentration. However, these elongated blebs are not necessarily pathological as they have been observed in motile cells.

Finally, we reiterate that each model is only valid within the parameter regions and physical limitations that have been discussed. By highlighting the benefits and restrictions of each model, we hope to have clarified the mathematical modelling landscape allowing the simplest model to be used when considering specific experimental cases.

Acknowledgements

AG is a Wolfson Royal Society Merit Holder and acknowledges support from a Reintegration Grant under EC Framework VII. TEW would like to thank St John's College Oxford for their financial support.

Funding

This publication is based on work supported by Award No. KUK-C1-013-04, made by King Abdullah University of Science and Technology (KAUST).

REFERENCES

- BERNFELD, S. R. & LAKSHMIKANTHAM, V. (1974) *An Introduction to Nonlinear Boundary Value Problems*. Mathematics in Science and Engineering. New York: Elsevier Science.
- BLASER, H., REICHMAN-FRIED, M., CASTANON, I., DUMSTREI, K., MARLOW, F. L., KAWAKAMI, K., SOLNICKA-KREZEL, L., HEISENBERG, C. P. & RAZ, E. (2006) Migration of zebrafish primordial germ cells: a role for myosin contraction and cytoplasmic flow. *Dev. Cell.*, **11**, 613–627.
- BUKORESHTLIEV, N. V., HAASE, K. & PELLING, A. E. (2013) Mechanical cues in cellular signalling and communication. *Cell. Tissue Res.*, **352**, 77–94.
- CHARRAS, G. T. (2008) A short history of blebbing. *J. Microsc.*, **231**, 466–478.
- CHARRAS, G. T., COUGHLIN, M., MITCHISON, T. J. & MAHADEVAN, L. (2008) Life and times of a cellular bleb. *Biophys. J.*, **94**, 1836–1853.
- CHARRAS, G. & PALUCH, E. (2008) Blebs lead the way: how to migrate without lamellipodia. *Nat. Rev. Mol. Cell Biol.*, **9**, 730–736.
- COLLINS-HOOPER, H., WOOLLEY, T. E., DYSON, L., PATEL, A., POTTER, P., BAKER, R. E., GAFFNEY, E. A., MAINI, P. K., DASH, P. R. & PATEL, K. (2012) Age-related changes in speed and mechanism of adult skeletal muscle stem cell migration. *Stem Cells*, **30**, 1182–1195.
- CUNNINGHAM, C. C. (1995) Actin polymerization and intracellular solvent flow in cell surface blebbing. *J. Cell Biol.*, **129**, 1589–1599.
- DAI, J. & SHEETZ, M. P. (1999) Membrane tether formation from blebbing cells. *Biophys. J.*, **77**, 3363–3370.
- EVANS, E. A. & SKALAK, R. (1980) *Mechanics and Thermodynamics of Biomembranes*. Boca Raton, FL: CRC Press.
- FACKLER, O. T. & GROSSE, R. (2008) Cell motility through plasma membrane blebbing. *J. Cell. Biol.*, **181**, 879.
- FUNKHOUSER, C. M., SKNEPNEK, R., SHIMI, T., GOLDMAN, A. E., GOLDMAN, R. D. & DE LA CRUZ, M. O. (2013) Mechanical model of blebbing in nuclear lamin meshworks. *Proc. Natl Acad. Sci.*, **110**, 3248–3253.
- GORIELY, A. (2013). personal communication.
- GORIELY, A., KÁROLYI, G. & TABOR, M. (2005) Growth induced curve dynamics for filamentary micro-organisms. *J. Math. Biol.*, **51**, 355–366.
- GORIELY, A. & TABOR, M. (2003a) Biomechanical models of hyphal growth in actinomycetes. *J. Theor. Biol.*, **222**, 211–218.
- GORIELY, A. & TABOR, M. (2003b) Self-similar tip growth in filamentary organisms. *Phys. Rev. Lett.*, **90**, 108101.
- GORIELY, A. & TABOR, M. (2006) Estimates of biomechanical forces in *Magnaporthe grisea*. *Mycol. Res.*, **110**(Pt 7), 755–759.
- HALLETT, M. B. & DEWITT, S. (2007) Ironing out the wrinkles of neutrophil phagocytosis. *Trends Cell Biol.*, **17**, 209–214.
- HALLETT, M. B., VON RUHLAND, C. J. & DEWITT, S. (2008) Chemotaxis and the cell surface-area problem. *Nat. Rev. Mol. Cell Bio.*, **9**, 662–662.
- HU, J. (2009) Mathematical modeling and analysis of in vitro actin filament dynamics and cell blebbing. *Ph.D. Thesis*, University of Minnesota.
- KELLER, H. U. & BEBIE, H. (1996) Protrusive activity quantitatively determines the rate and direction of cell locomotion. *Cell Motil. Cytoskeleton*, **33**, 241–251.
- KELLER, H. & EGGI, P. (1998) Protrusive activity, cytoplasmic compartmentalization, and restriction rings in locomoting blebbing Walker carcinosarcoma cells are related to detachment of cortical actin from the plasma membrane. *Cell Motil. Cytoskeleton*, **41**, 181–193.

- LIM, F. Y., CHIAM, K. H. & MAHADEVAN, L. (2012) The size, shape, and dynamics of cellular blebs. *B. Am. Phys. Soc.*, **55**, 28004–28010.
- MAUGIS, B., BRUGUÉS, J., NASSOY, P., GUILLEN, N., SENS, P. & AMBLARD, F. (2010) Dynamic instability of the intracellular pressure drives bleb-based motility. *J. Cell. Sci.*, **123**, 3884–3892.
- NICHOL, J. A. & HUTTER, O. F. (1996) Tensile strength and dilatational elasticity of giant sarcolemmal vesicles shed from rabbit muscle. *J. Phys.*, **493**, 187.
- OTTO, A., COLLINS-HOOPER, H., PATEL, A., DASH, P. R. & PATEL, K. (2011) Adult skeletal muscle stem cell migration is mediated by a blebbing/amoeboid mechanism. *Rejuvenation Res.*, **14**, 249–260.
- POZRIKIDIS, C. (2001) Effect of membrane bending stiffness on the deformation of capsules in simple shear flow. *J. Fluid. Mech.*, **440**, 269–291.
- PRESSLEY, A. (2010) *Elementary Differential Geometry*. Springer Undergraduate Mathematics. Berlin: Springer.
- PROTHERO, J. W. & SPENCER, D. (1968) A model of blebbing in mitotic tissue culture cells. *Biophys. J.*, **8**, 41–51.
- RUSSELL, S. W., ROSENAU, W. & LEE, J. C. (1972) Cytolysis induced by human lymphotoxin: cinemicrographic and electron microscopic observations. *Am. J. Pathol.*, **69**, 103.
- SAHAI, E. & MARSHALL, C. J. (2003) Differing modes of tumour cell invasion have distinct requirements for Rho/ROCK signalling and extracellular proteolysis. *Nat. Cell. Biol.*, **5**, 711–719.
- SHEETZ, M. P., SABLE, J. E. & DÖBEREINER, H. G. (2006) Continuous membrane-cytoskeleton adhesion requires continuous accommodation to lipid and cytoskeleton dynamics. *Annu. Rev. Biophys. Biomol. Struct.*, **35**, 417–434.
- SIDELL, B. D. & HAZEL, J. R. (1987) Temperature affects the diffusion of small molecules through cytosol of fish muscle. *J. Exp. Biol.*, **129**, 191–203.
- SKALAK, R., TOZEREN, A., ZARDA, R. P. & CHIEN, S. (1973) Strain energy function of red blood cell membranes. *Biophys. J.*, **13**, 245–264.
- SPANGLER, E. J., HARVEY, C. W., REVALEE, J. D., SUNIL KUMAR, P. B. & LARADJI, M. (2011) Computer simulation of cytoskeleton-induced blebbing in lipid membranes. *Phys. Rev. E*, **84**, 051906.
- STRYCHALSKI, W. & GUY, R. (2012) A computational model of bleb formation. *Math. Med. Biol.*, **12**, 462.
- TINEVEZ, J. Y., SCHULZE, U., SALBREUX, G., ROENSCH, J., JOANNY, J. F. & PALUCH, E. (2009) Role of cortical tension in bleb growth. *Proc. Natl Acad. Sci.*, **106**, 18581–18586.
- TONGEN, A., GORIELY, A. & TABOR, M. (2006) Biomechanical model for appressorial design in *Magnaporthe grisea*. *J. Theor. Biol.*, **240**, 1–8.
- TOZLUOĞLU, M., TOURNIER, A. L., JENKINS, R. P., HOOPER, S., BATES, P. A. & SAHAI, E. (2013) Matrix geometry determines optimal cancer cell migration strategy and modulates response to interventions. *Nat. Cell. Biol.*, **15**, 751–762.
- WOOLLEY, T. E., GAFFNEY, E. A., OLIVER, J. M., BAKER, R. E., WATERS, S. L. & GORIELY, A. (2014) Cellular blebs: pressure-driven, axisymmetric, membrane protrusions. *Biomech. Model. Mechan.*, **13**, 463–476.
- YOSHIDA, K. & SOLDATI, T. (2006) Dissection of amoeboid movement into two mechanically distinct modes. *J. Cell. Sci.*, **119**, 3833–3844.
- YOUNG, J. & MITRAN, S. (2010) A numerical model of cellular blebbing: a volume-conserving, fluid-structure interaction model of the entire cell. *J. Biomech.*, **43**, 210–220.